



Optics Letters

Photoacoustic and hyperspectral dual-modality endoscope

NING LIU,¹ SIHUA YANG,^{1,2} AND DA XING^{1,*}

¹MOE Key Laboratory of Laser Life Science and Institute of Laser Life Science, College of Biophotonics, South China Normal University, Guangzhou 510631, China

²e-mail: yangsh@scnu.edu.cn

*Corresponding author: xingda@scnu.edu.cn

Received 5 October 2017; revised 24 November 2017; accepted 1 December 2017; posted 1 December 2017 (Doc. ID 308566); published 22 December 2017

We have developed a dual-modality endoscope composed of photoacoustic (PA) and hyperspectral imaging, capable of visualizing both structural and functional properties of bio-tissue. The endoscope's composition and scanning mechanism was described, and the feasibility of the dual-modality endoscope was verified by mimic phantom experiments. Lately, we demonstrated its endoscopic workability through *in vivo* experiments. The experimental results showed that the proposed herein hybrid endoscope can provide optical imaging of the surface and tomography imaging for the deeper features, and a functional oxygen saturation rate map of the same imaging area. We demonstrated optical-resolution PA imaging of vascular structures and an oxygen saturation rate map in a rabbit's rectum. It confirmed that this dual-modality endoscope can play an important role in comprehensive clinical applications. © 2017 Optical Society of America

OCIS codes: (110.4234) Multispectral and hyperspectral imaging; (170.5120) Photoacoustic imaging; (170.2150) Endoscopic imaging.

<https://doi.org/10.1364/OL.43.000138>

Because current tools and techniques for diagnosing lower digestive tract and urogenital diseases, such as human rectum, endometrial, and prostate cancers, are inadequate, more effective and accurate means are needed in a clinical setting [1]. A video-endoscope system such as standard white light endoscope and narrow-band imaging (NBI) techniques are mandatory for the early examination, allowing the collection of images of the entire lower digestive tract and providing diagnostic information such as changes in color and irregularity of surface mucosa [2–4]. Hyperspectral imaging (HSI) has especially been an emerging modality for medical application in recent years [5]. HSI provides a continuous, essentially complete record of the spectral responses of biotissues over certain wavelength ranges and renders the information in image form [6]. However, owing to its limited imaging penetration depth, subsurface morphology information is still missing for complete and comprehensive inspection.

Photoacoustic endoscopy (PAE) embodies photoacoustic (PA) tomography in a miniaturized probe to enable high-resolution imaging of internal organs with optical absorption contrast [7]. PAE provides structural information by visualizing blood vasculature as well as dye-labeled lymph nodes *in vivo*, and also allows high-resolution interrogation much deeper than an optical endoscope [8–10]. In particular, multispectral photoacoustic tomography can identify hemoglobin and other tissue chromophores, revealing pathophysiological aberrations *in vivo* [11,12], yet the relatively low imaging speed is one of the major bottlenecks for fast functional optical resolution (OR)-PAE. In recent years, a number of differently sized PA imaging probes have been reported, such as intravascular [13] and a urogenital endoscope [14]. However, those probes are all used in a stand-alone form, without the incorporation of a video endoscopic function. Therefore, seeking to achieve more comprehensive diagnostic information, we first proposed and realized a dual-modality endoscope composed of photoacoustic and HSI. First, the new system is capable of a HSI modality realized by measuring the back-scattered light of the sample. We can obtain the relative oxygen saturation rate map through a modified spectral unmixing method. Second, optical resolution PA imaging can provide biological structural information below the intestinal wall. By combining these two imaging modalities, we can extend the imaging depth, and get fast functional imaging and tomography imaging in endoscopic applications.

In this Letter, we have successfully demonstrated the ability of the dual-modality endoscope through mimic phantom and *in vivo* experiments. To verify the photoacoustic imaging mode, an agar phantom was prepared, and the resolution and imaging depth presented here were expected. Then we imaged a nude mouse's ear to verify that HSI could visualize microvascular structures and provide a corresponding oxygen saturation rate map. Finally, to demonstrate the endoscope's *in vivo* imaging ability, we imaged the rectum of a New Zealand white rabbit. Our study showed that the proposed herein hybrid endoscope system can gain optical imaging of the surface and tomography imaging for the deeper features, and an oxygen saturation rate map of the same imaging area.

Figure 1(a) shows the endoscope's peripheral systems. PA mode comprises an exciting light source, an ultrasonic receiver,

a signal amplifier, and a data acquisition (DAQ) system and a variety of optics. The light source for PA signal excitation is a miniature laser (Model DTL-314QT, pulsed Q -switched lasers, Russia) that delivers 4 ns laser pulses at a wavelength of 532 nm with a repetition rate of 10 KHz. The exciting laser beam is collimated by a telescope system and then coupled into the endoscope's single-mode fiber through an optical fiber coupler (FiberPort, Thorlabs). The collected PA signals are sequentially amplified with a 50 dB low-noise amplifier (LNA-650, RFBAY) and digitized by a data acquisition (DAQ) card (M3i.4110, SPECTRUM) and stored in the computer's hard drive for later data processing. HSI mode comprises an illumination source, a CCD camera, an objective lens, a liquid crystal tunable filter (LCTF), and a light transmitting bundle. The illumination light source used here is a 350 W quartz tungsten halogen (QTH) broadband source (GL350-5, SHENDA endoscope, China). The camera used to collect hyperspectral images is a 3.0 megapixel CCD camera (MSHOT, China). Spectral response of this camera is from 400 nm to 1000 nm, covering the wavelength range of the LCTF. Broadband light was delivered into the LCTF through a fiber bundle. A collimated light beam through the filter became a series of single wavelength transmission light ranging from 400 nm to 750 nm with a 5 nm increment. Monochromatic light then coupled into a fiber bundle transmit to the distal end of the endoscope for tissue illumination. After tissue illumination, the backscattered light from the surface is transmitted by relay optics and finally collected by the camera. While in HSI mode, since the objective lens is arranged at a 45° angle to the probe's central shaft, it can cover only a portion of the inner wall.

Figure 1(b) shows the detailed schematic of the dual-mode endoscope. A custom-made Grin-lens with a diameter of 2 mm

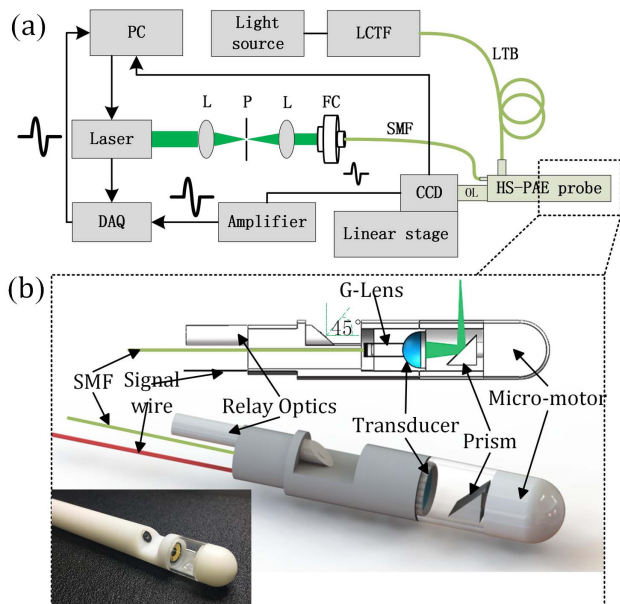


Fig. 1. Schematic of the PA-HSI endoscope system. (a) Schematic illustration of the imaging setup with alignment of various modules. Abbreviations: DAQ, data acquisition system; CCD, charge-coupled device; L, lens; P, pinhole; FC, fiber coupler; OL, objective lens; LCTF, liquid crystal tunable filter; SMF, single-mode fiber; LTB, light transmitting bundle. (b) Architecture and photography of the endoscope. SMF, single-mode fiber; G-lens, grin-lens.

and a focal distance of 12 mm is attached to the distal end of the single-mode fiber (SMF). Such an arrangement makes the illumination focus about 1 mm above the probe's outer surface. The SMF is coaxially placed in the center of an ultrasound transducer, a 15 MHz polyvinylidene fluoride (PVDF) transducer with a 150% bandwidth. The transducer is spherically focused with a curvature radius of 15 mm, leading to a 17 mm effective focusing length. At the center of the transducer is a 2 mm small hole containing the distal end of the exciting fiber. After exiting the optical fiber, the focused exciting laser beam is reflected by the prism and sent to the target tissue to generate PA signals. The generated PA signals first pass through an optically and acoustically transparent polyethylene terephthalate membrane and then are reflected by the prism reflector before being detected by the ultrasonic transducer. The prism is coated with silver to reflect both excitation light and PA signals. Via the Grin-lens and spherically focused transducer, laser pulses and acoustic waves are delivered and received coaxially to achieve an efficient overlap of the illumination and acoustic detection. All parts are coaxially aligned and sealed in the imaging chamber filled with nonconducting silicone oil. To record B-scan PA signals, the prism is fixed on the rotation shaft of a micromotor (Once Top Motor, China). To support the micromotor, we fabricated a bridge-shape frame and mounted the micromotor at the distal end of the frame. The motor's signal wire passed through the bridge section and connected to the motor drive. Because of the bridge section, the angular field-of-view (FOV) of the endoscope is partially blocked by 120° . The rotation speed of the micromotor can be up to 10 rps. In the imaging experiments to be presented later, since the micromotor is immersed in silicone oil, we record data with a 5 Hz B-scan frame rate to avoid distinct vibration. We utilize a high-speed digitizer. Considering the large probe diameter of 12 mm, we record 800 A-lines per B-scan, leading to an angular step size of 0.45° for the scanning mirror. For 3D imaging, the probe is mounted on a 1D motor stage. By linearly pulling the probe, we can acquire sectional images of different locations along the axial direction.

The feasibility of the PA mode was first validated by experiments using phantoms composed of 2% agar and ink with a light absorption coefficient of 0.007 mm^{-1} and reduced scattering coefficient of 0.7 mm^{-1} . Four $100 \mu\text{m}$ thick glass capillaries filled with blood were inserted into the phantom. Figure 2(a) showed a schematic illustration of the phantom. Two capillaries were closer to the inner surface and parallel to the central axis, the other two were located 1 mm from the inner surface. Figure 2(b) showed a PA B-scan image of the dashed circle line in (a). As the target moved away from the focus point (i.e., Positions 3 and 4), because of the optical focusing degradation with depth the transverse resolution deteriorates. The line spread function (LSF) was calculated as the derivative of the PA B-scan signal. In Fig. 2(d), we present radial LSFs for the target located at the focal point. Based on the LSFs, we determined the endoscope's radial resolution to be $60 \mu\text{m}$ in the radial direction, respectively. The FWHM of the LSF defining the highest transverse resolution was estimated to be $40 \mu\text{m}$, as shown in Fig. 2(e). Figure 2(c) was a 3D-rendered PA image of the phantom, a complete structure of the two capillaries located at the focal point was shown clearly. Owing to transverse resolution deterioration with depth, the other two capillaries' image became blurred, but we could still

get an actual structural morphology and hence verified PA imaging ability. The maximum imaging depth of the PA mode was estimated to be 2 mm.

For HSI mode, we established a relationship between the concentration of the tissue chromophores and their corresponding absorbance intensity values [15]. The raw data had first been normalized to address the problem of the spectral nonuniformity of the illumination device and the influence of the dark current. After this preprocessing step, the calculation of the absolute attenuation of light in the tissue was by the equation

$$A = \log\left(\frac{I_{\text{cal_LCTF}}}{I_{\text{cal_tissue}}}\right), \quad (1)$$

where A is the tissue attenuation, $I_{\text{cal_tissue}}$ is the calibrated tissue image, and $I_{\text{cal_LCTF}}$ is the calibrated light intensity through LCTF. These data are acquired at discrete wavelength bands; A can be expressed as a function of wavelength-dependent attenuation factors. Using a modified version of the Lambert–Beer law to account for the effects of scattering, the absorption can be expressed as follows:

$$A(\lambda) = b_0 + b_1\mu_{\text{eff}}(\lambda) + \varepsilon_{\text{oxyHb}}(\lambda)c_{\text{oxyHb}} + \varepsilon_{\text{deoxy}}(\lambda)c_{\text{deoxyHb}}. \quad (2)$$

Notice that in this case, oxygenated and deoxygenated hemoglobin are generally used. μ_{eff} is the effective attenuation coefficient derived from diffusion theory [15],

$$\mu_{\text{eff}}(\lambda) = 0.244 + 85.3e^{-\left(\frac{\lambda-154}{66.2}\right)},$$

calculated for representative biotissue optical properties at each wavelength, and it accounts for attenuation due to nonhemoglobin absorption and scattering, with b_1 being a free parameter modulating the magnitude of this term. b_0 is a constant term accounting for overall changes in signal due to spectral reflection, source intensity, and so on. $\varepsilon_i(\lambda)$ gives the extinction coefficient of the absorber as a function of wavelength. A linear nonnegative least squares fitting algorithm is used to extract the terms b_0 , b_1 , and c_i , on a pixel by pixel basis. In this case, c_i is a composite term that is effectively the product of the concentration and path length of light attenuated by each absorber. This enables

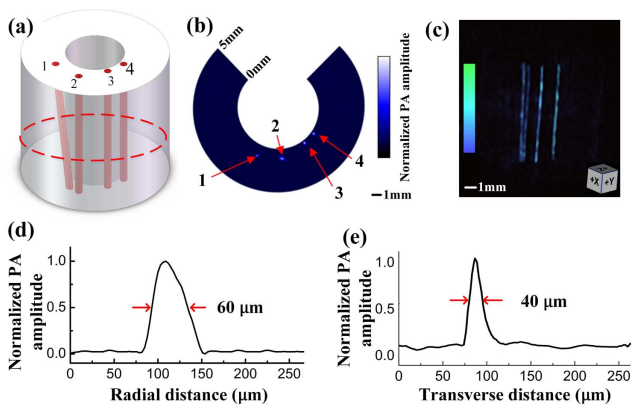


Fig. 2. Resolution evaluation and phantom imaging results obtained by PA mode. (a) Schematic illustration of the agar phantom. (b) PA B-scan image of the 100 μm thick glass capillaries located at four locations. (c) PA volumetric image of the glass capillaries in the agar phantom. (d) Hilbert-transformed signal (radial LSF) of typical PA A-line signal for the glass capillary. (e) Transverse LSF of the 100 μm thick glass capillary located at the focal point (Position 3).

quantification of the relative total hemoglobin (Hb) content \times path length product as $c_{\text{oxyHb}} + c_{\text{deoxyHb}}$, where these correspond to deoxygenated Hb and oxygenated Hb, respectively. The hemoglobin oxygen saturation rate is calculated as (the path length term cancels out) follows:

$$s\text{O}_2 = \frac{c_{\text{oxyHb}}}{c_{\text{oxyHb}} + c_{\text{deoxyHb}}} \times 100\%. \quad (3)$$

To verify the performance in estimating $s\text{O}_2$, *in vivo* imaging of the microvascular structure and oxygen saturation rate in a nude mouse's ear using HSI mode was shown in Fig. 3. Figure 3(a) was part of the raw hyperspectral images of the mouse's ear, we had 66 images in total from 420 nm to 750 nm with an average 5 nm wavelength increment. The imaging region of interest was 4 mm \times 4 mm. Hyperspectral images were acquired sequentially for different wavelengths using an integration time of 100 ms to 300 ms per wavelength. Differences in integration times compensated for signal loss caused by the spectral output of the source, tissue optical properties, and optical losses due to the tunable filter. Using the spectral unmixing method described above, we quantified oxygen saturation rate pixel by pixel. Figure 3(b) showed the corresponding oxygen saturation rate map of the mouse's ear. Anesthesia effects may have caused overall lower than normal oxygen levels.

To further demonstrate the endoscope's imaging ability, we imaged the rectum of a New Zealand white rabbit (Harlan) *in vivo*. The rabbit fasted for 10 h before the experiment to create an empty colon for imaging. For this experiment, we performed the experiment *in vivo* after anesthetizing the animal (pentobarbital, 150 mg/kg, IP injection) to avoid possible complications. We cleansed the rabbit's colon with a saline laxative enema and spread water into the colon for acoustic coupling. Then we inserted the probe into the colon and performed endoscopic imaging with a B-scan imaging speed of 5 Hz and a laser pulse energy of 0.55 mJ at 4 KHz repetition rate, yielding an optical fluence of 13 mJ/cm² (65% of the ANSI safety limit of 20 mJ/cm²). To achieve volumetric imaging, we recorded B-scan images during the constant pullback translation of the probe (10 $\mu\text{m}/\text{s}$) provided by a motorized translation stage. Since these two imaging modes were working independently, we could obtain PA and HSI imagers simultaneously. But due to the movement of blood and slight vibration caused by the scanning motor, artifacts were created in calculating the oxygen saturation rate throughout the vasculature.

Therefore, during the PA imaging process, HSI mode worked in a standard white light illumination condition.

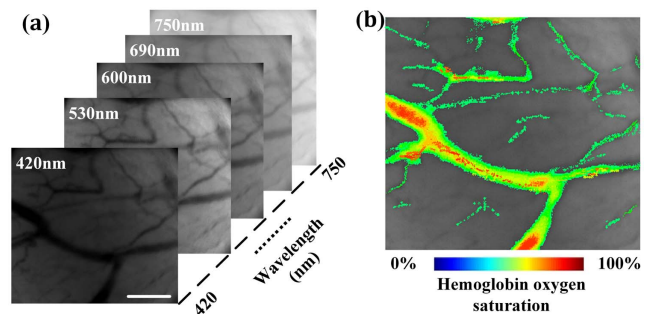


Fig. 3. HSIs and hemoglobin oxygen saturation map of a nude mouse's ear *in vivo*. (a) Parts of the raw HSIs of a mouse's ear. Scale bar 1 mm. (b) HSI of percent hemoglobin oxygen saturation.

When reaching regions of interests, we temporarily stopped the collection of PA signals about 10 s to complete HSI mode. All procedures in the animal experiments followed protocols approved by the Institutional Animal Care and Use Committee at South China Normal University in Guangzhou.

Figure 4(a) was a PA radial maximum amplitude projection (RMAP) image acquired *in vivo* over a 10 mm range with a 12 mm image diameter and (b) was the corresponding 3D volumetric image. The 3D volumetric image was obtained by scanning the probe cylindrically over 360° and linearly along the sample longitudinal dimension over 10 mm, with the rectal wall and the probe kept close to each other during scanning. As can be seen, the PA image resolved the large vessels, which accurately matched those visible in the photograph. Numerous smaller vessels were not clearly distinguishable in the HSI image that can be seen in the PA image. Notice that in Fig. 4(a) some of the microvascular structures on the left and bottom of the image showed some discontinuity, we speculated that the distortions were caused by the nonuniform coupling. Figures 4(c) and 4(d) were two HSIs of the rabbit's rectum, marked with a dashed rectangle in Fig. 4(a). Notice that HSIs presented here were blurry because the objective lens' working distance was a fixed value and hence may have been out of focus. Using the spectral unmixing method described in Eq. (1), we quantified the oxygen saturation rate pixel by pixel. Figures 4(c₁) and 4(d₁) showed the corresponding oxygen saturation rate map of (c) and (d). As shown in Fig. 4(c₁), the sO₂ values along the capillaries gradually changed from high to low when the RBCs flow from the arterioles to the venules. The oxygen level in arterioles and venules showed in Fig. 4(c₁) was in good agreement with other reports. Figures 4(c₂) and 4(d₂) showed PA B-scan images of the indicated dashed line in (a), respectively, with Fig. 4(c₂) corresponding to the lower

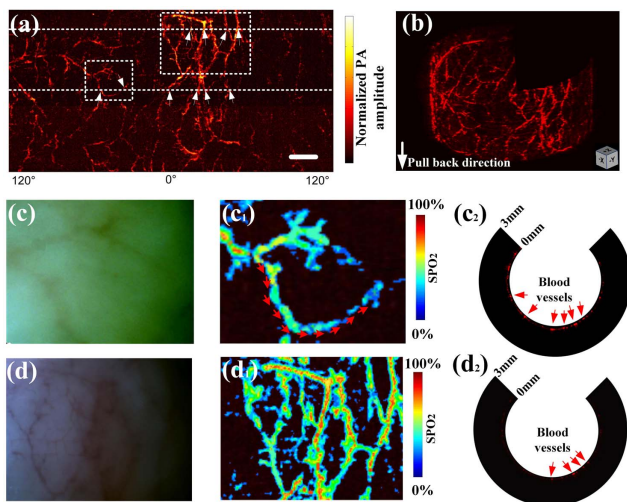


Fig. 4. Photoacoustic and HSIs of rabbit's rectum *in vivo*. (a) Radial maximal amplitude projection images acquired in PA mode from a rabbit rectum acquired *in vivo* over a 10 mm range with a 12 mm image diameter. Scale bar 1 mm. (b) PA volumetric image of the same region. (c) and (d) are two images of the rabbit's rectum from the dashed rectangle in (a), (c) corresponding to the small rectangle area and (d) indicating the larger rectangle area. (c₁) and (d₁) Corresponding oxygen saturation rate map of (c) and (d). (c₂) and (d₂) PA B-scan image of the indicated dashed line in (a), respectively.

line and Fig. 4(d₂) indicating the upper line. These PA images showed the cross-sections of blood vessels distributed in the intestine wall, which was estimated to be ~2 mm thick.

The data presented herein demonstrate for the first time, to the best of our knowledge, the feasibility of a hybrid photoacoustic and hyperspectral endoscope. HSI mode provides not only visual images among visible light band but also differences in absorption and reflection at molecular levels. In particular, HSI can recover multiple physiological parameters, not only Hb and HbO₂, and more physiological parameters such as cholesterol, different kinds of lipids can also be recovered if near-infrared spectrum or exogenous markers are used. This indicates HSI can be used for more complex biomedical applications such as tumor or atherosclerosis detection. The PA imaging mode can provide vascular structure information under the surface layer. It should be noted that about 120 deg of view is missing in PA mode, and imaging speed of PA mode is not fast enough for meeting the real-time imaging needs. Using a higher repetition rate laser source and a more powerful motor may improve the imaging speed. And the missing imaging degree could be narrowed down with a more compact configuration design. Besides, owing to the fixed working distance of the objective lens as well as vibration caused by the micromotor, HSIs become blurred and reduce the resolution. To improve the applicability of the presented endoscope, an objective lens with adjustable focal length should be applied. Further work will be carried out to explore the potential of the fused technology.

Funding. National Natural Science Foundation of China (NSFC) (11604105, 11774101, 61627827, 81630046, 91539127); Science and Technology Planning Project of Guangdong Province, China (2015B020233016); Distinguished Young Teacher Project in Higher Education of Guangdong, China (YQ2015049); Science and Technology Youth Talent for Special Program of Guangdong, China (2015TQ01X882).

REFERENCES

- S. A. Cannistra and J. M. Niloff, *New Engl. J. Med.* **334**, 1030 (1996).
- H. Tajiri, K. Matsuda, and J. Fujisaki, *Dig. Endosc.* **14**, 131 (2002).
- M. A. Kara, F. P. Peters, W. D. Rosmolen, K. K. Krishnadath, F. J. ten Kate, P. Fockens, and J. J. Bergman, *Endoscopy* **37**, 929 (2005).
- H. Machida, Y. Sano, Y. Hamamoto, M. Muto, T. Kozu, H. Tajiri, and S. Yoshida, *Endoscopy* **36**, 1094 (2004).
- G. L. Lu and B. W. Fei, *J. Biomed. Opt.* **19**, 010901 (2014).
- K. J. Zuzak, S. C. Naik, A. George, H. Doyle, B. Khosrow, and E. H. Livingston, *Anal. Chem.* **79**, 4709 (2007).
- L. V. Wang and S. Hu, *Science* **335**, 1458 (2012).
- A. Taruttis and V. Ntziachristos, *Nat. Photonics* **9**, 219 (2015).
- J. M. Yang, K. Maslov, H. C. Yang, Q. Zhou, K. K. Shung, and L. V. Wang, *Opt. Lett.* **34**, 10 (2009).
- H. L. He, G. Wissmeyer, S. V. Ovsepian, A. Buehler, and V. Ntziachristos, *Opt. Lett.* **41**, 2708 (2016).
- A. Taruttis, G. M. van Dam, and V. Ntziachristos, *Cancer Res.* **75**, 1548 (2015).
- Z. J. Chen, S. H. Yang, and D. Xing, *Opt. Lett.* **37**, 3414 (2012).
- X. R. Ji, K. D. Xiong, S. H. Yang, and D. Xing, *Opt. Express* **23**, 9130 (2015).
- C. Li, J. Yang, R. Chen, C. Yeh, L. Zhu, K. Maslov, Q. Zhou, K. K. Shung, and L. V. Wang, *Opt. Lett.* **39**, 1473 (2014).
- G. M. Palmer, A. N. Fontanella, S. Shan, G. Hanna, G. Zhang, C. L. Fraser, and M. W. Dewhirst, *Nat. Protoc.* **6**, 1355 (2011).